SUPPORTING INFORMATION FOR:

Enhancing the adhesion between Self-Assembled Molecules and perovskite Enabled 22.6% efficiency for Flexible Solar Cells

Qiqing Luo,[a] Yanqing Zhu,[a] Ning Teng,[b] Yijie Wang,[a] Xinyan Hou,[a] Min Hu,[c] Wenchao Huang,[d] Wenping Yin,[e]* and Jianfeng Lu[a]*

[a] State Key Laboratory of Silicate Materials for Architectures, Wuhan University of Technology, Wuhan 430070, China;

[b] 7533 Research Institute, R&D Center, Qingdao GAOCE Technology Co., Ltd. 215000 Qingdao, China;

[c] School of Electronic and Electrical Engineering, Hubei Province Engineering Research Center for Intelligent Micro-Nano Medical Equipment and Key Technologies, Wuhan Textile University, Wuhan 430200, China;

[d] School of Materials Science and Engineering, Wuhan University of Technology, Wuhan 430070, China;

[e] College of Physics and Optoelectronic Engineering, Harbin Engineering University, Qingdao 266000, China.

*E-mail: jianfeng.lu@whut.edu.cn

SUPPORTING INFORMATION

TABLE OF CONTENTS **Page**

EXPERIMENTAL PROCEDURES

Materials. Formamidinium iodide (FAI) and was purchased from Greatcell Solar Materials Pty Ltd. NiO_x nanoparticles was purchased from Advanced Election Technology Co., Ltd. Lead iodide (PbI_2) and Me-4PACz were purchased from TCI. The CPP-2PACz was synthesized by our lab. Lead bromide ($PbBr_2$), bathocuproine (BCP) and C60 were purchased from Xi'an Yuri Solar Technology. Methylammonium chloride (MACl) was synthesized according to previous reports.[1, 2] N, N-Dimethylformamide (DMF), Dimethyl sulfoxide (DMSO), and isopropanol (IPA) were purchased from Sigma Aldrich. All materials were directly used without further purification.

Synthesis. A mixture of diethyl (2-(12-phenylindolo[2,3-a]carbazol-11(12*H*)-yl)ethyl)phosphonate (approx. 0.9 mmol), 1,4-dioxane (15 mL), and bromotrimethylsilane (10.1 mmol) was stirred under nitrogen atmosphere after three cycles of evacuation and nitrogen refilling. The reaction proceeded at 25 ℃ for 24 h, then quenched by methanol. Deionized water was added and the mixture was stirred for additional 3 h. The crude product was collected by filtration and purified by recrystallization to afford CPP-2PACz.[6]

Device fabrication. The PEN|ITO substrates were prepared by initial etching with a nanosecond laser machine, followed by ultrasonic cleaning using detergent, deionized water, and EtOH for 15 min in each medium. Subsequently, the substrates were dried in the oven for 20 min and treated with ultraviolet ozone (UVO) for 15 min before use.

Hole transporting layer (HTL): 10 mg NiO_x nanoparticles were dispersed in 1 mL of isopropanol-water mixtures at volume ratio (IPA: H_2O = 1:3). To improve the dispersion, 40 mol% H_2O_2 was added to suspensions. Then, the prepared solution was deposited by using spin-coating method (3000 rpm for 30 s with an acceleration of 2000 rpm·s^{-1}), followed by annealing at 140 ºC for 20 min in ambient air. CPP-2PACz (0.5 mg·ml^{-1} in isopropanol) was deposited on the NiO_x at 3000 rpm for 30 s, followed by annealing at 100 ºC for 10 min. The deposition method of Me-4PACz was consistent with CPP-2PACz.

Perovskite layer: 1.45 M $FA_{0.9}Cs_{0.1}PbI_{2.85}Br_{0.15}$ perovskite precursor solution was prepared by mixing FAI, PbI_2, $PbBr_2$, and CsI in a DMF/DMSO (v: v = 4:1) mixed solvent, and 15 mol%

MACl was added into precursor for controlling the perovskite growth. Then, the obtained precursor solutions were filtered through a 0.2 μm PTFE filter. The resulted solution was spin-coated onto the substrates at 1000 rpm for 10 s and 5000 rpm for 30 s, and 130 μL ethyl acetate was dripped as the anti-solvent at the final 10 s before the finishing of spinning. Then, the perovskite films were annealed at 100 ºC for 60 min.

Surface passivation layer: 0.4 $mg \cdot ml^{-1}$ Piperazinehydroiodide (PI) dissolved in IPA was coated on perovskite surface at 5000 rpm for 30s, and annealed at 100 ºC for 5 min.

Electron transporting layer (ETL): ETL were deposited by vacuum thermal deposition of C60 (23 nm), BCP (8 nm) at a rate of 0.1-0.2 $Å \cdot s^{-1}$ in a high vacuum chamber ($< 4 \times 10^{-4}$ Pa). 90 nm Ag was thermally evaporated at a rate of 1 $Å \cdot s^{-1}$ in a high vacuum chamber ($< 5 \times 10^{-4}$ Pa) through a metal shadow mask (aperture area: 0.16 cm^2).

Characterization

^{1}H NMR and *^{13}C NMR* spectra were recorded by a Bruker AV400 Spectrometer operating at 500 MHz and 126 MHz.

High-resolution mass spectra (HRMS) was obtained in negative electrospray ionization (ESI) mode utilizing a Thermo Scientific Q-Exactive Plus mass spectrometer.

Thermogravimetric analysis (TGA) was measured by utilizing a TGA8000+Spectrum 3.

Ultraviolet–visible spectroscopy (UV-vis) absorption spectra were obtained using a UV-vis spectrophotometer (LambDA 750s, PerkinElmer).

X-ray diffraction (XRD) patterns were recorded with a PANalytical B.V Empyrean diffractometer using a Cu K_α X-ray tube operating at 40 kV, 40 mA, with a step size of 0.013° and a step time of 0.12 s.

X-ray Photoelectron Spectroscopy (XPS) measurements were performed on a Thermo Scientific ESCALAB Xi+ using 200W monochromated Al K_α (1486.6 eV) radiation. A 500 μm X-ray spot was used for XPS analysis. Typically, the hydrocarbon C 1s line at 284.8 eV from adventitious carbon was used for energy referencing.

Scanning electron microscopy imaging (SEM) was recorded by a ZEISS GeminiSEM 300 to study the top-view and cross-sectional images of perovskite films and devices.

Steady-state photoluminescence (PL) and Time resolved PL(TRPL) were measured with a 485 nm picosecond pulsed diode laser (HORIBA Scientific Company, Japan; Nano LED-C2 N-485L). The impulse energy is 14 pJ/pulse, and the excitation laser intensity is 70 mW. The emission signals was collected and collimated with an off-axis parabolic mirror (HORIBA; 1427C) and measured with a DSS LN Solid State (DSS) detector (HORIBA; 1427C). A 550 nm longpass filter (Thorlabs; FELH0550) was employed to suppress scattered laser excitation. Photon arrival times were recorded via a time-correlated single photon counting card (Fluoromax-4; TCSPC) and all data analysis was performed in Origin.

External Quantum Efficiency (EQE) measurements were performed using an external quantum efficiency tester from Newport, USA (PT-QEM1000). A photodiode employed for calibrate the EQE setup was calibrated by Newport.

Current–voltage characteristics were measured using a Keithley source meter combined with an Oriel solar simulator equipped with a xenon lamp (100 $mW \cdot cm^{-2}$) and an AM 1.5G filter. A non-reflective metal aperture with an area of 0.16 cm^2 was adopted to define the irradiation area. *J–V* curves were recorded with a scan speed of 100 $mV \cdot s^{-1}$ scanning from short circuit to forward bias (-0.1 V → 1.2 V) and forward bias to short circuit (1.2 V → -0.1 V) directions. The forward bias to short circuit scan measurements always immediately followed the short circuit to forward bias scan. Quasi-stabilized power output (q-SPO) was monitored for 120 s at the potential corresponding to the maximum power point in the reverse *J-V* curve (1.2 V→-0.1 V).

The extraction process of activation energy (E_a): Firstly, absorption spectroscopy was employed to determine the time *t* required for the complete nucleation and crystallization of perovskite. The perovskite growth rate *k* was then derived as 1/*t*. Subsequently, the growth rates at different temperatures were fitted to the Arrhenius equation (S1), yielding a linar relationship between 1/*RT* and ln(t), where the slope of the line corresponds to the activation energy E_a.

$$\ln(k) = -E_a\frac{1}{RT} + C \tag{S1}$$

Surface energy can be calculated by following steps. Based on the geometric mean rule describing dispersive forces between pairs of unlike molecules, the work of adhesion (W_a) between a liquid and a solid in contact is given by the following equation (S2):[3]

$$W_a = \gamma_{SV} + \gamma_{LV} - \gamma_{SL} \quad \text{(S2)}$$

where γ_{SV}, γ_{LV} and γ_{SL} denote the surface energy, liquid-vapor surface tension, and solid–liquid interface tension. The correlation between solid-liquid interfacial tension, the surface tensions of both phases and the contact angle θ is given by The Young equation (S3):[4]

$$\gamma_{SV} = \gamma_{SL} + \gamma_{LV} cos\theta \quad \text{(S3)}$$

Combining equation (S2) and (S3) yields equation (S4):

$$W_a = \gamma_{LV}(1 + cos\theta) \quad \text{(S4)}$$

W_a can also be expressed in terms of the polarity and dispersion components of the two phases, as shown in equation (S5):[5]

$$W_a = 2\sqrt{\gamma_{SV}^d \gamma_{LV}^d} + 2\sqrt{\gamma_{SV}^p \gamma_{LV}^p} \quad \text{(S5)}$$

where $\gamma p\ LV$ and $\gamma d\ LV$ represent the polar and dispersive components of liquid surface tension, $\gamma p\ SV$ and $\gamma d\ SV$ correspond to polar and dispersive components of surface energy. Substitution of these parameters into the combined equation (S6) enables the derivation of $\gamma p\ SV$ and $\gamma d\ SV$:

$$\gamma_{LV}(1 + cos\theta) = 2\sqrt{\gamma_{SV}^d \gamma_{LV}^d} + 2\sqrt{\gamma_{SV}^p \gamma_{LV}^p} \quad \text{(S6)}$$

The table shows the known $\gamma p\ LV$ and $\gamma d\ LV$ of the two liquids, and the contact angles of the two liquids is shown in the Table S1.

Liquid	γ_{LV} (mN/m)	$\gamma d\ LV$ (mN/m)	$\gamma p\ LV$ (mN/m)
Water	72.8	21.8	51.0
Ethylene glycol	48.3	29.3	19.0
Methane diiodide	48.5	48.5	0

Finally, the surface energy can be obtained by:

$$\gamma_{SV} = \gamma_{SV}^{p} + \gamma_{SV}^{d} \tag{S7}$$

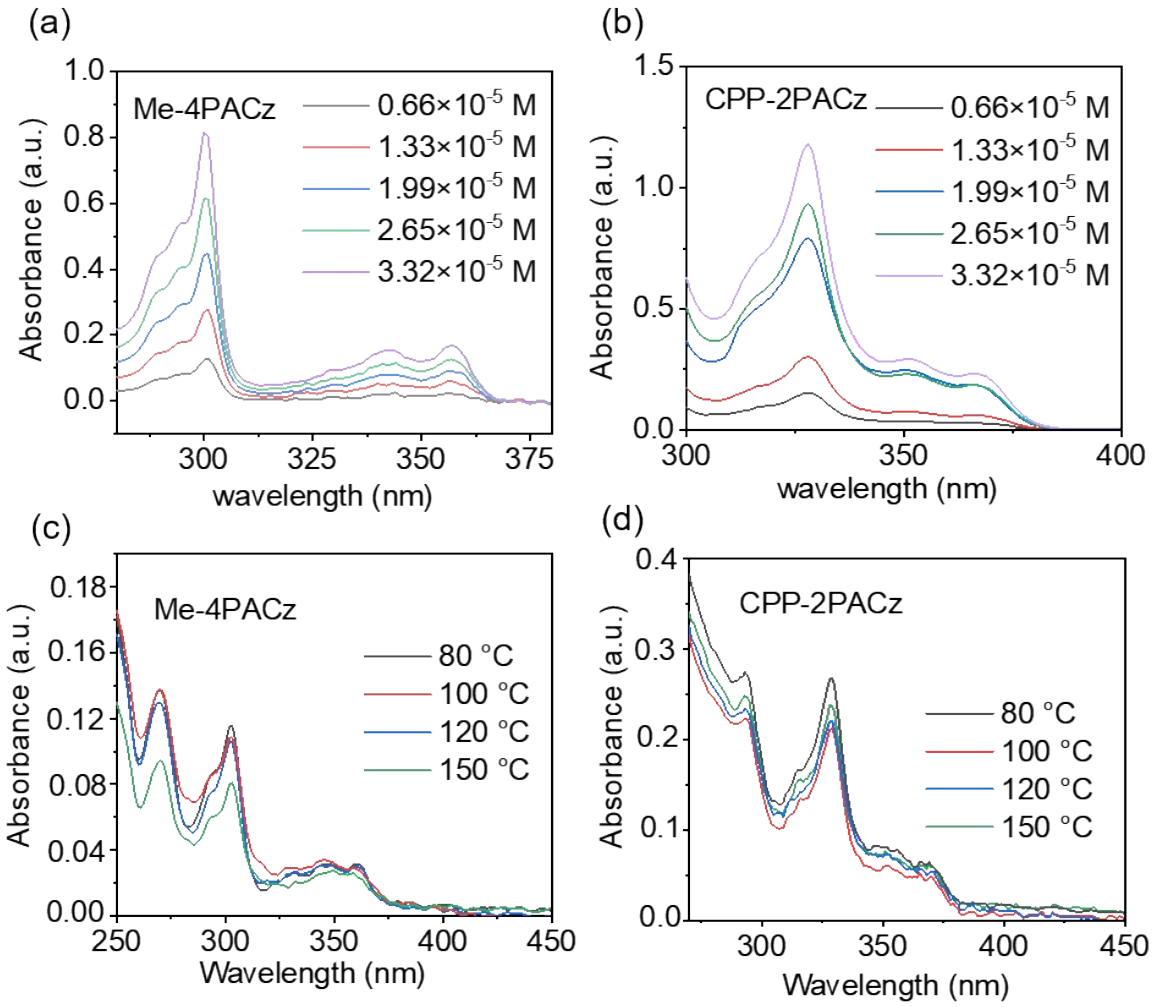

Figure S1. UV-vis absorption spectra of SAMs in alkaline solution (pH=10): (a) Me-4PACz, and (b) CPP-2PACz. UV–vis absorption spectra of SAM films de-adsorbed by basic solution (pH = 10): (c) Me-4PACz, and (d) CPP-2PACz.

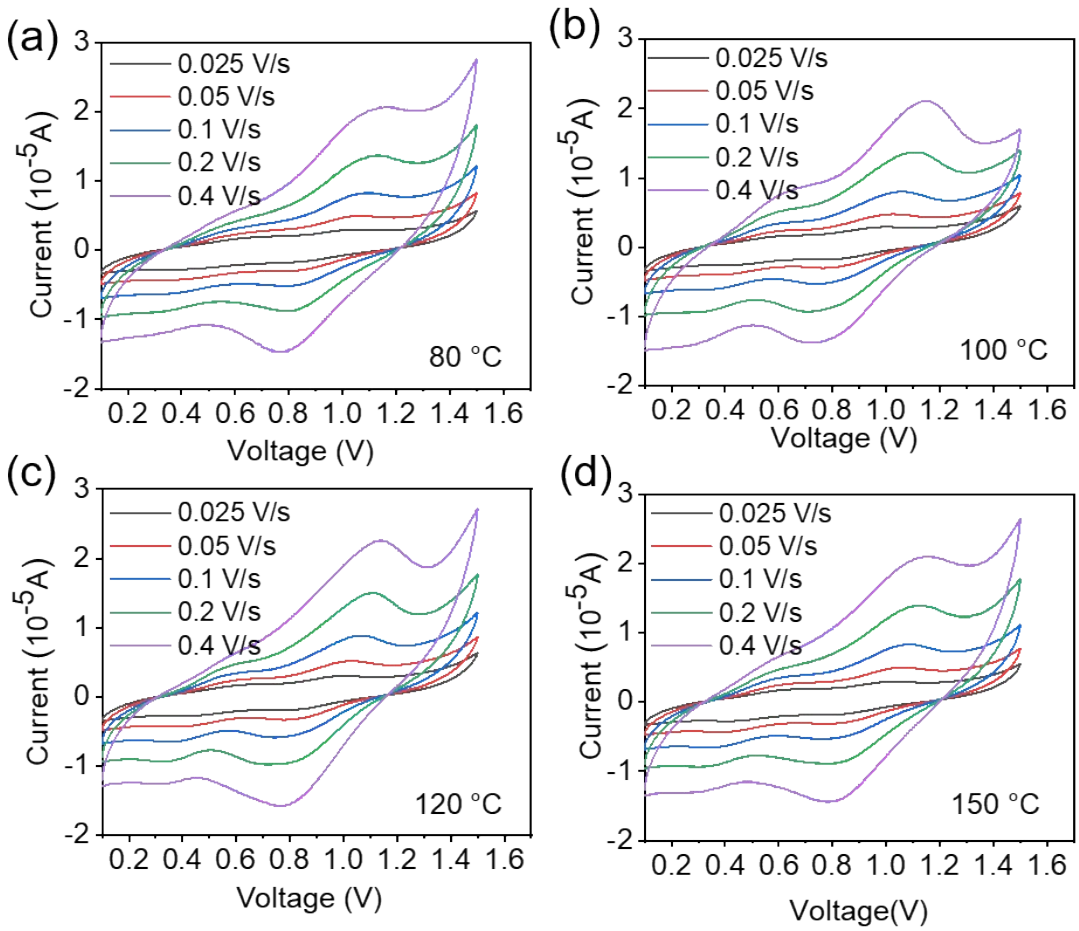

Figure S2. Cyclic voltammograms of Me-4PACz on PEN|ITO|NiO_x substrates measured in o-DCB solution under different scan rates.

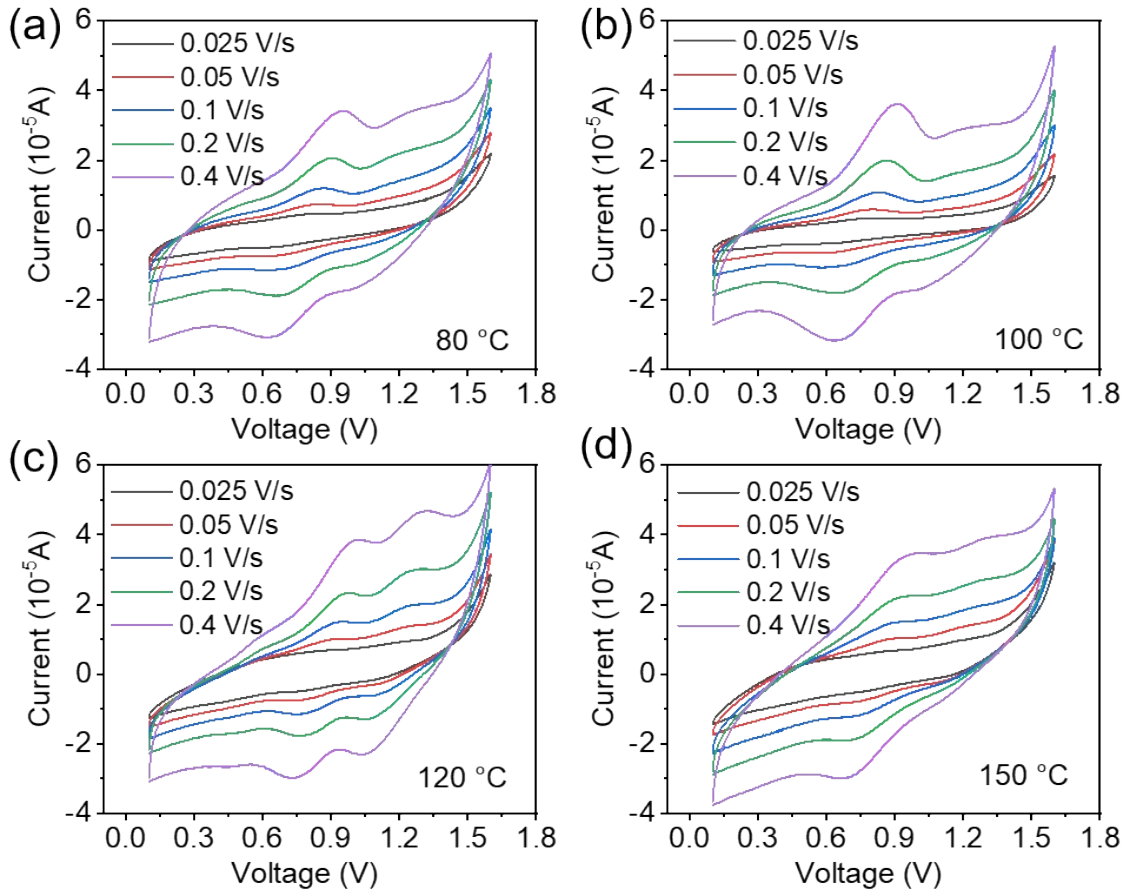

Figure S3. Cyclic voltammograms of CPP-2PACz on PEN|ITO|NiO_x substrates.

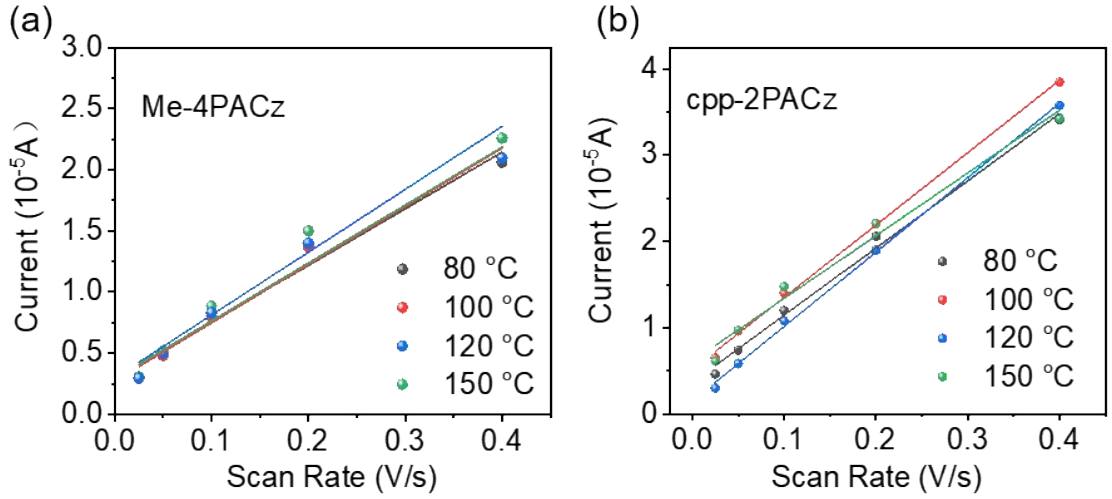

Figure S4. The peak current vs. scanning rate in cyclic voltammetry measurements of SAMs with different annealing temperatures.

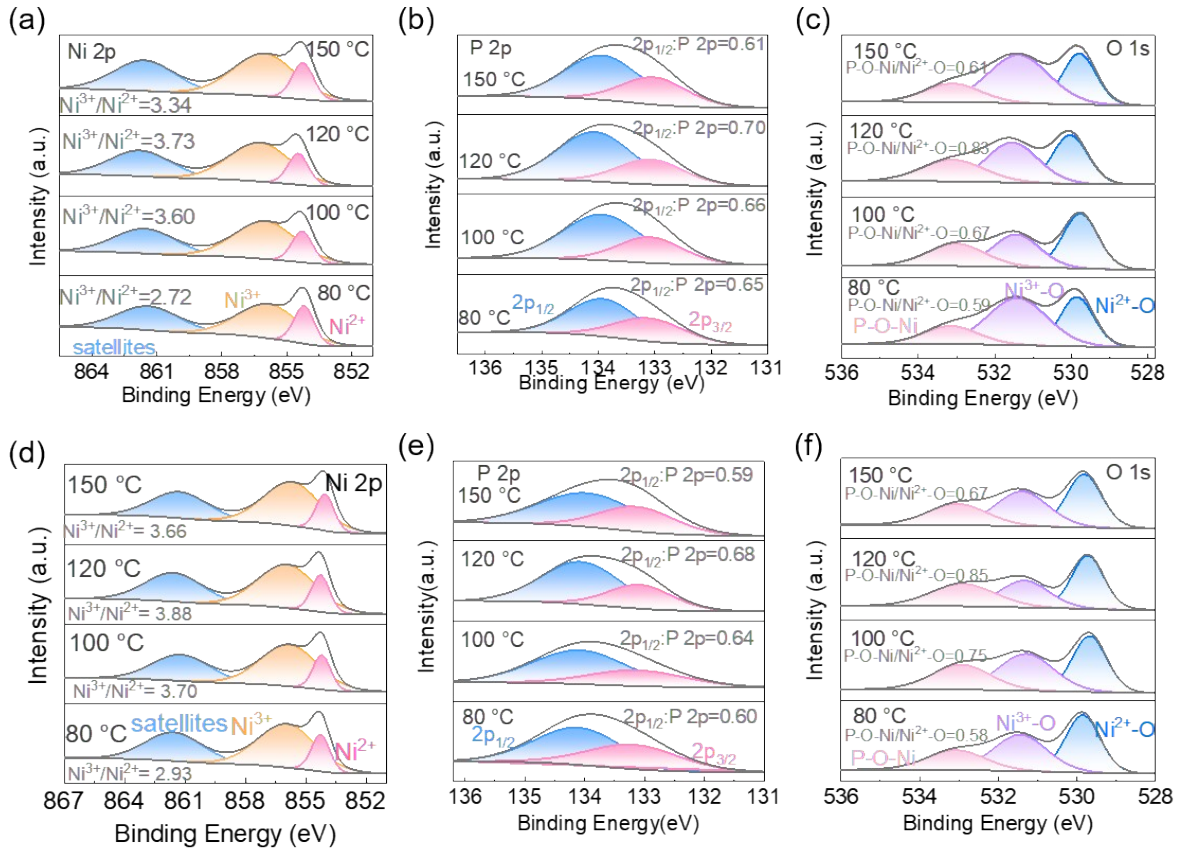

Figure S5. XPS spectra of characteristic elements of Me-4PACz annealed at different temperatures: (a) Ni 2p; (b) P 2p; (c) O 1s. XPS spectra of characteristic elements of CPP-2PACz annealed at different temperatures: (d) Ni 2p; (e) P 2p; (f) O 1s. The structure is PEN|ITO|NiO_x|SAMs.

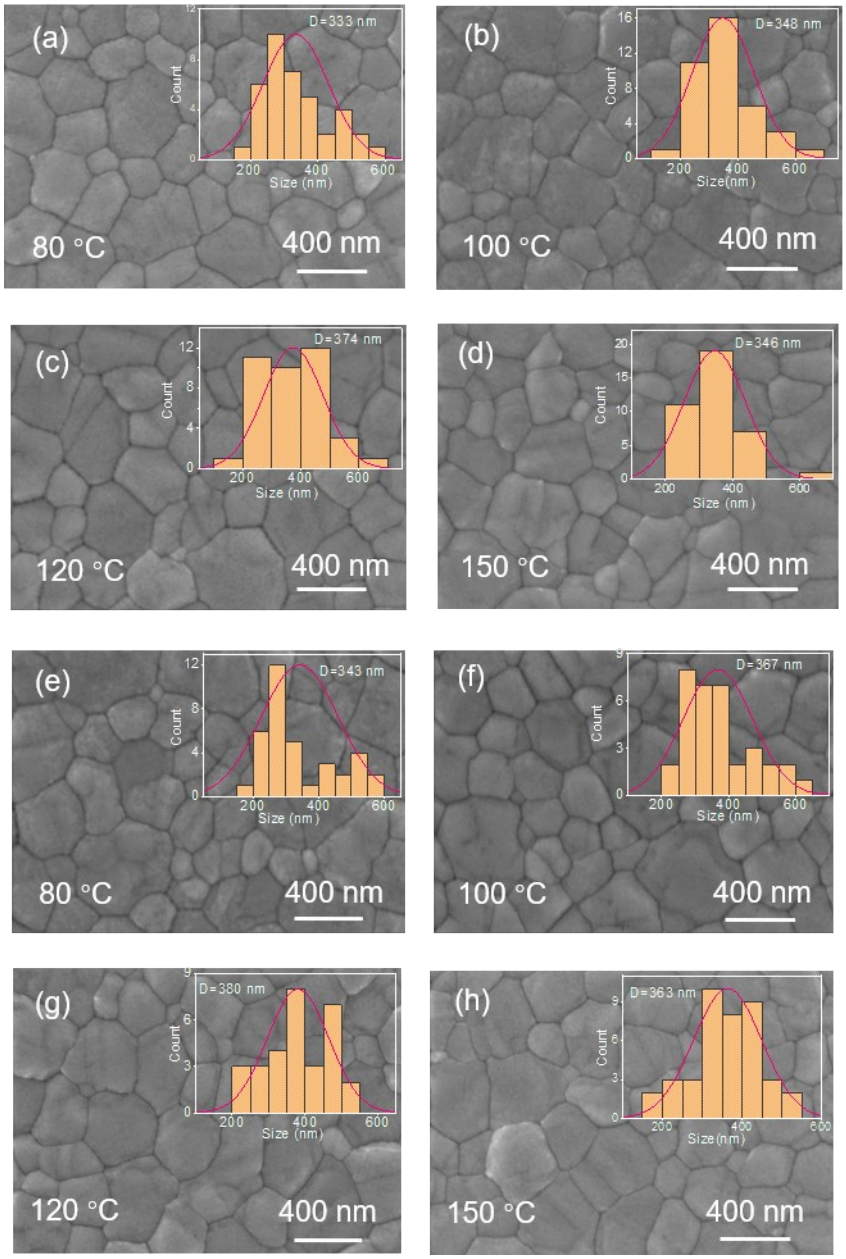

Figure S6. SEM images and grain size statistics of the perovskite top surface on Me-4PACz annealed at (a) 80 °C, (b) 100 °C, (c) 120 °C, and (d)150 °C. SEM images and grain size statistics of the perovskite top surface on CPP-2PACz annealed at (e) 80 °C, (f) 100 °C, (g) 120 °C, and (h) 150 °C. The structure is PEN|ITO|NiO_x|SAMs|perovskite.

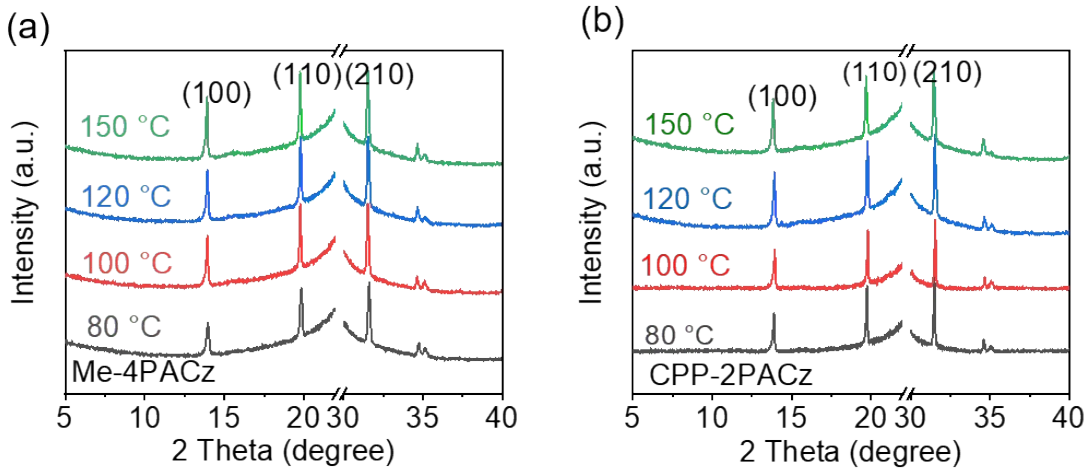

Figure S7. XRD patterns of the top surface of perovskite films: (a) Me-4PACz, and (b) CPP-2PACz. The structure is PEN|ITO|NiO_x|SAMs|$FA_{0.9}Cs_{0.1}PbI_{2.85}Br_{0.15}$.

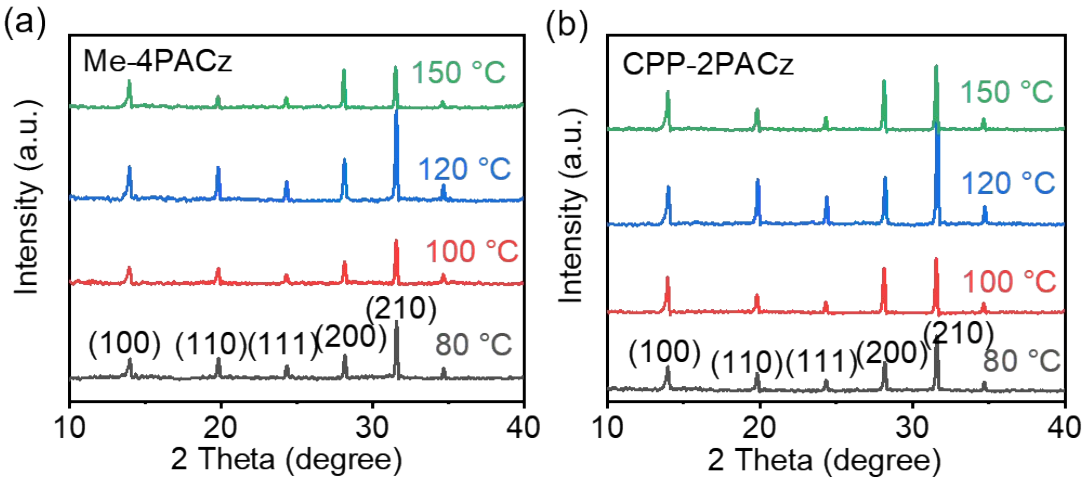

Figure S8. XRD patterns of the buried surface of perovskite films: (a) Me-4PACz, and (b) CPP-2PACz. The structure is PEN|ITO|NiO_x|SAMs|$FA_{0.9}Cs_{0.1}PbI_{2.85}Br_{0.15}$.

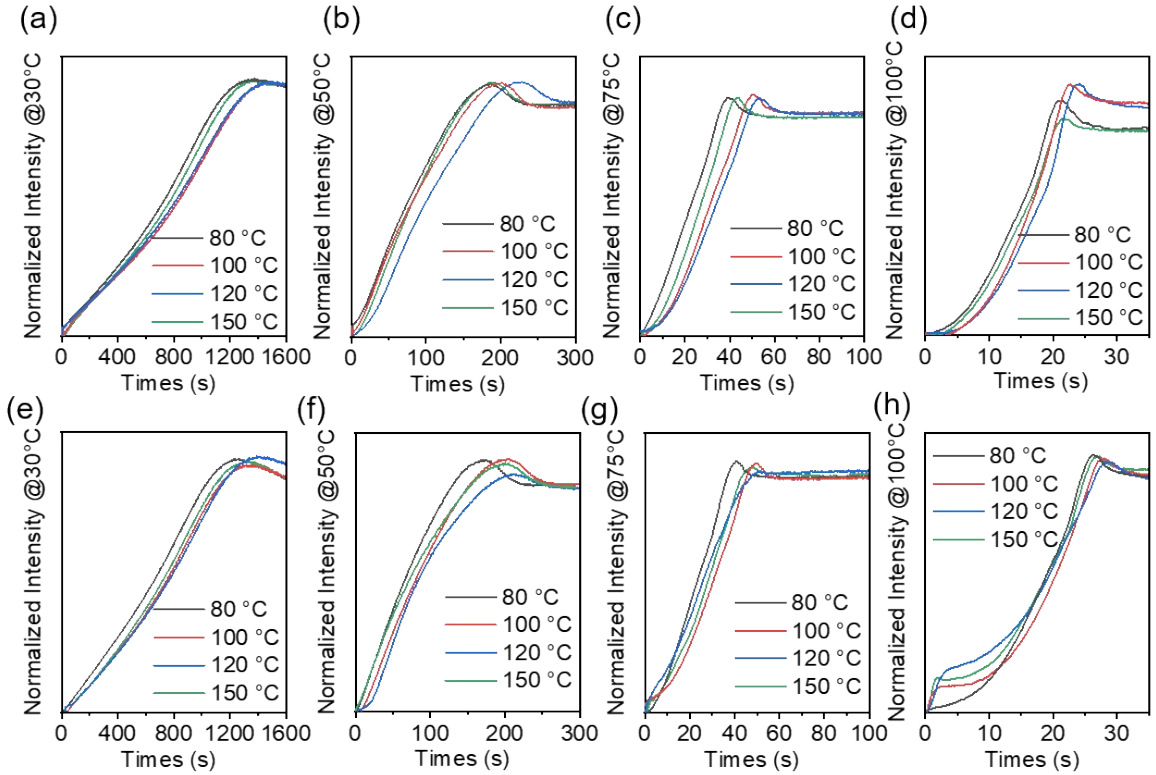

Figure S9. The evolution of the UV–vis absorptivity (at 730 nm) of perovskite precursor deposited on different SAMs. The annealing temperature of the perovskite at a) 30 °C, b) 50 °C, c) 75 °C, and d) 100 °C on Me-4PACz; The annealing temperature of the perovskite at e) 30 °C, f) 50 °C, g) 75 °C, and h) 100 °C on CPP-2PACz. The structure is PEN|ITO|NiO_x|SAMs|perovskite.

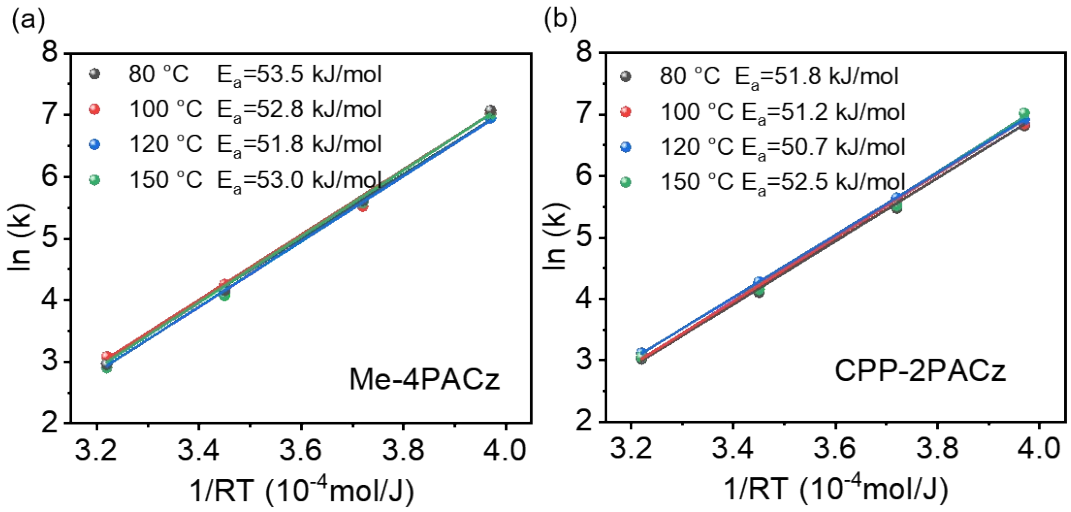

Figure S10. Plots constructed from equation (2) to extract E_a needed for the perovskite growth on SAMs annealed at different temperatures. (a) Me-4PACz, and (b) CPP-2PACz. The structure is PEN|ITO|NiO_x|SAMs|perovskite.

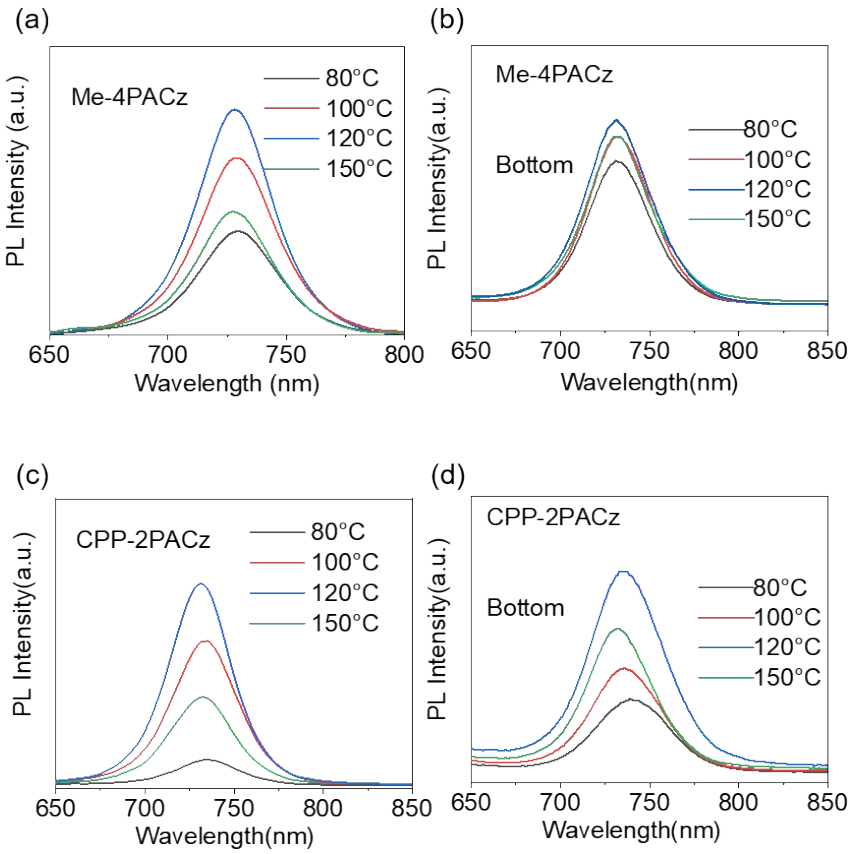

Figure S11. PL of the perovskite on Me-4PACz: (a) top surface, and (b) bottom surface; PL of the perovskite on CPP-2PACz: (c) top surface and (d) bottom surface. The structure is PEN|ITO|NiO_x|SAMs|perovskite.

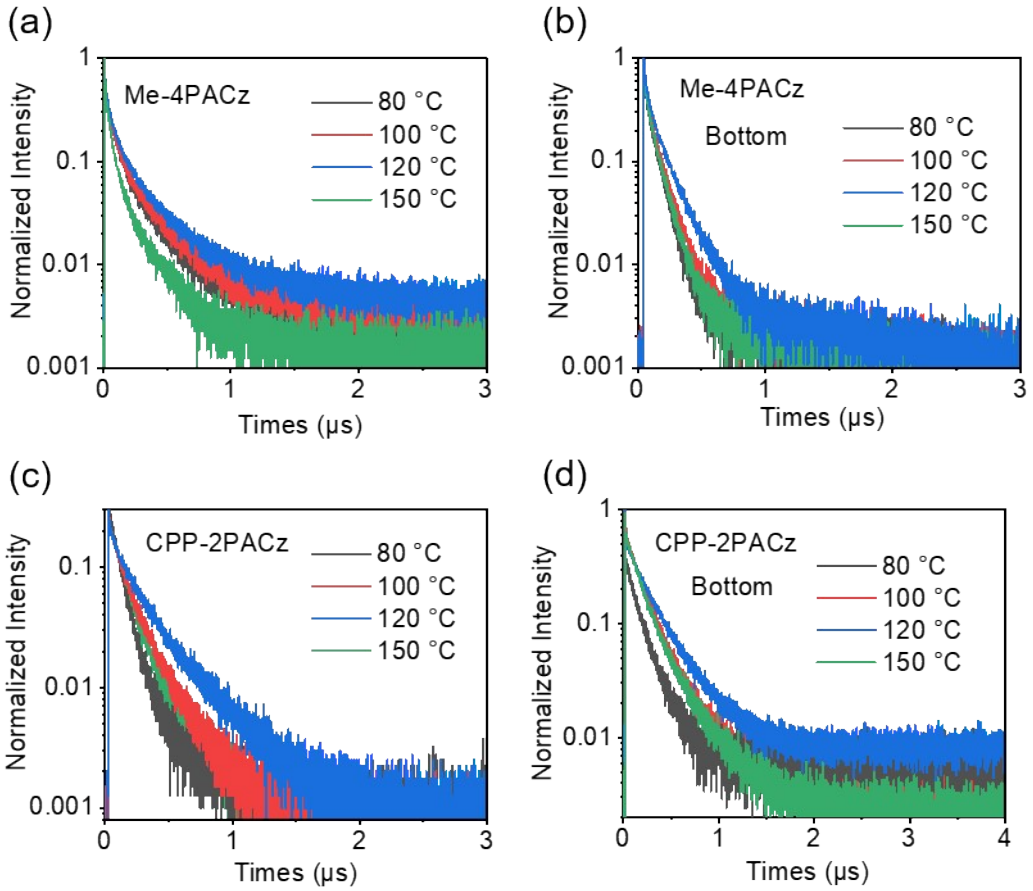

Figure S12. TRPL of the perovskite on Me-4PACz: (a) excited from the top surface side, and (b) excited from bottom surface side; TRPL of the perovskite on CPP-2PACz: (c) excited from the top surface side and (d) excited from the bottom surface side. The structure is PEN|ITO|NiO_x|SAMs|perovskite.

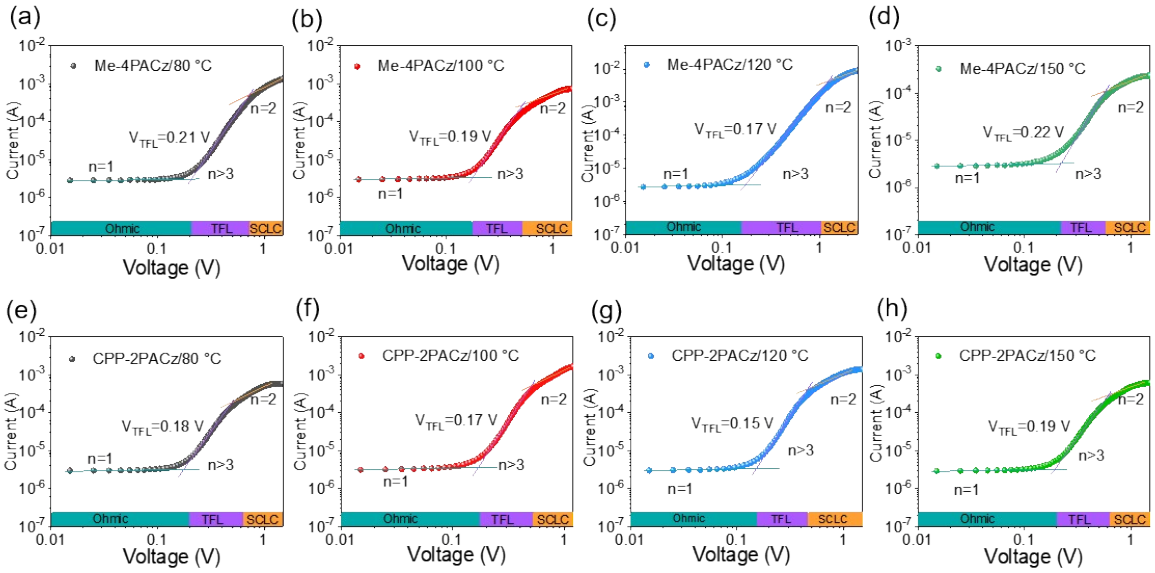

Figure S13. The SCLC curves of perovskite devices deposited on (a-d) Me-4PACz and (e-h) CPP-2PACz annealed at different temperatures. The sample structure is PEN|ITO|NiO_x|SAMs|perovskite|spiro-OMeTAD|Ag.

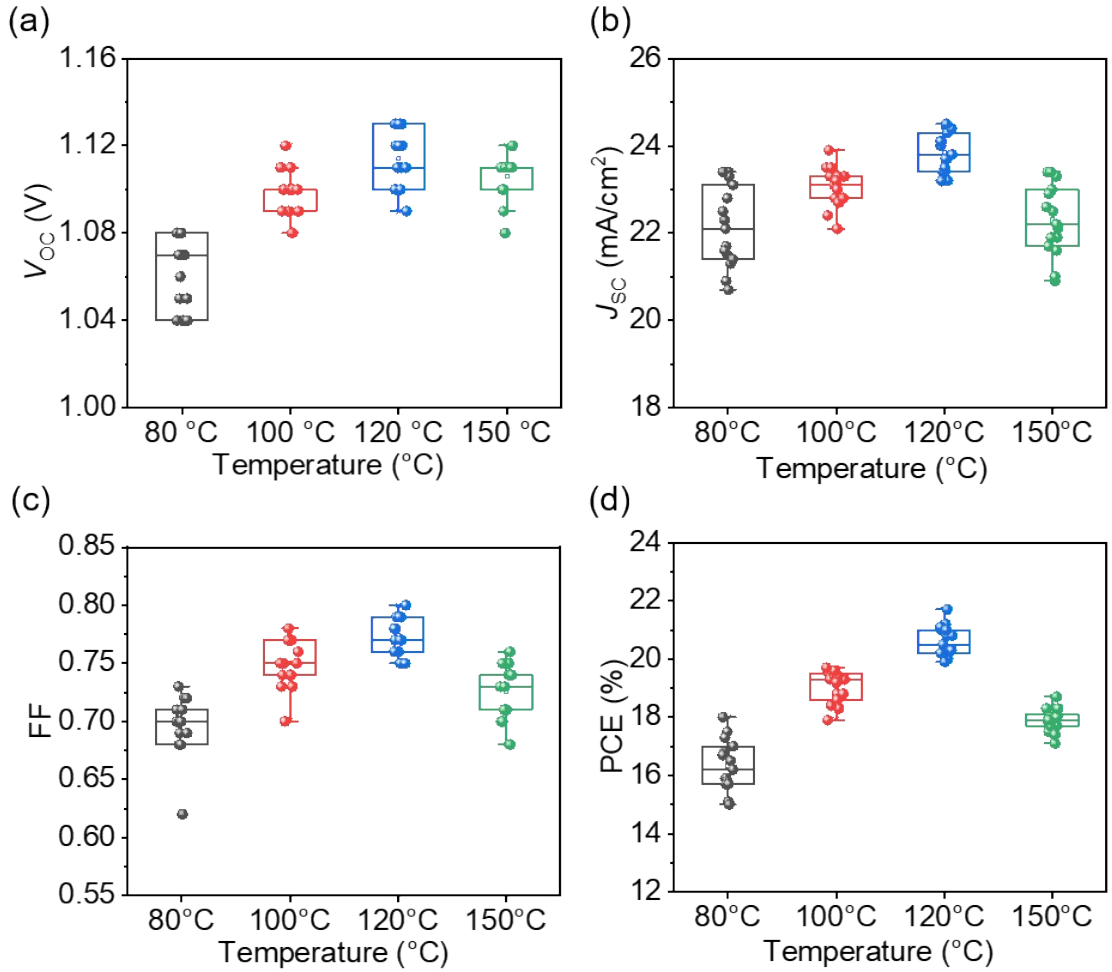

Figure S14. Statistics of the (a) V_{OC}, (b) J_{SC}, (c) FF, and (d) PCE distribution of F-PSCs based on Me-4PACz. The device structure is PEN|ITO| NiO_x|Me-4PACz|perovskite|C60|BCP|Ag. The photovoltaic parameters are obtained under AM 1.5G 1-sun irradiation with active areas of 0.16 cm^2.

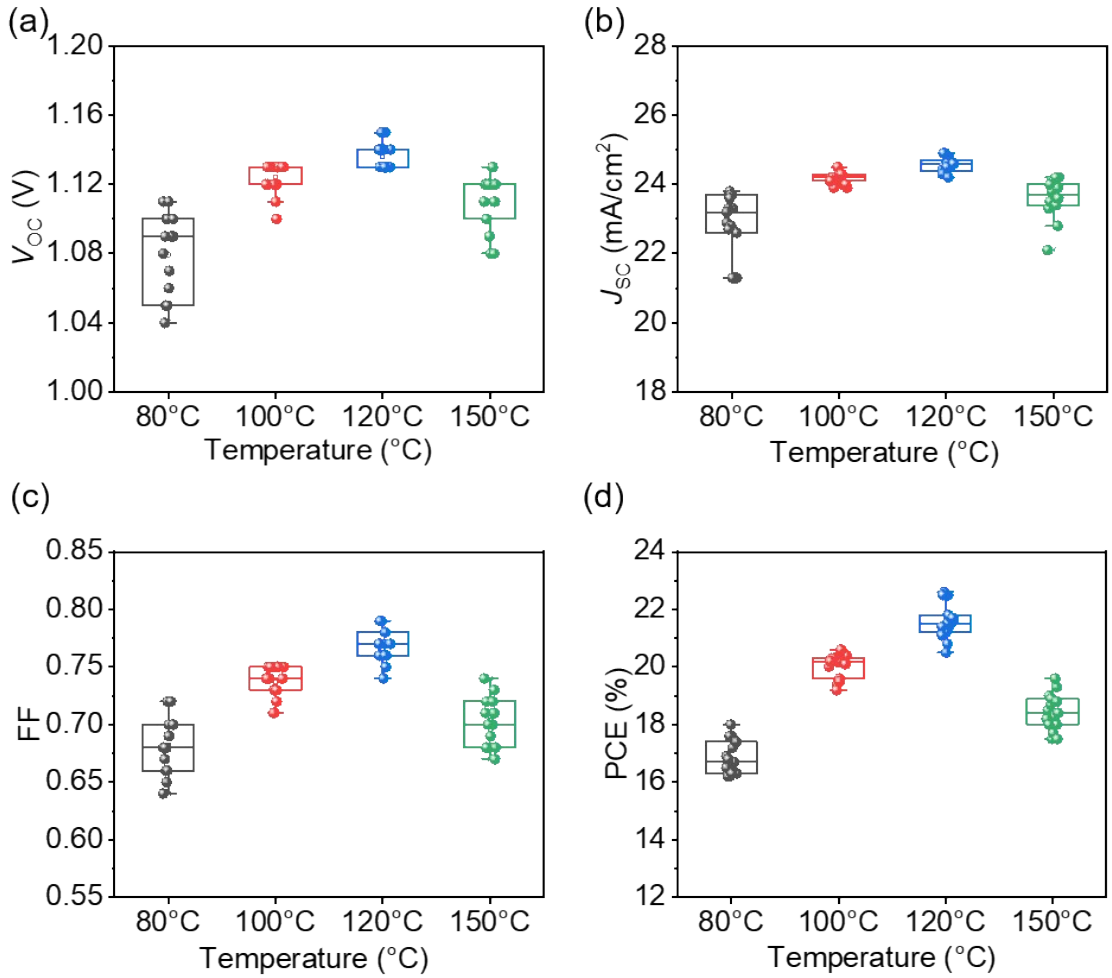

Figure S15. Statistics of the (a) V_{OC}, (b) J_{SC}, (c) FF, and (d) PCE distribution of F-PSCs based on CPP-2PACz. The device structure is PEN|ITO|NiO_x|CPP-2PACz|perovskite|C60|BCP|Ag. The photovoltaic parameters are obtained under AM 1.5G 1-sun irradiation with active areas of 0.16 cm^2.

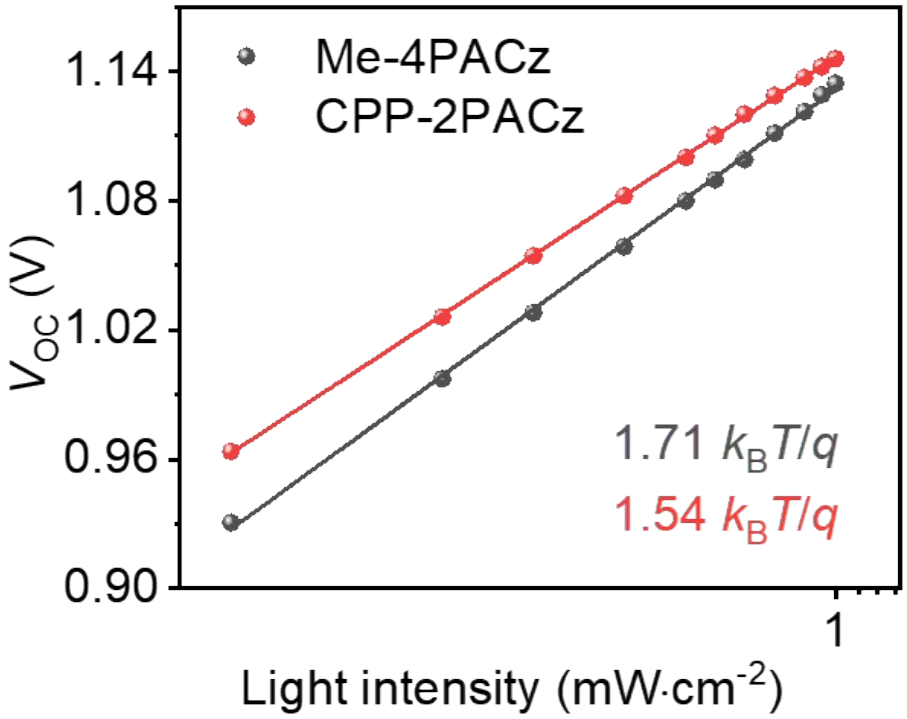

Figure S16. Plot of open-circuit voltage versus light intensity. The device structure is PEN|ITO|NiO_x|SAMs|perovskite|C60|BCP|Ag.

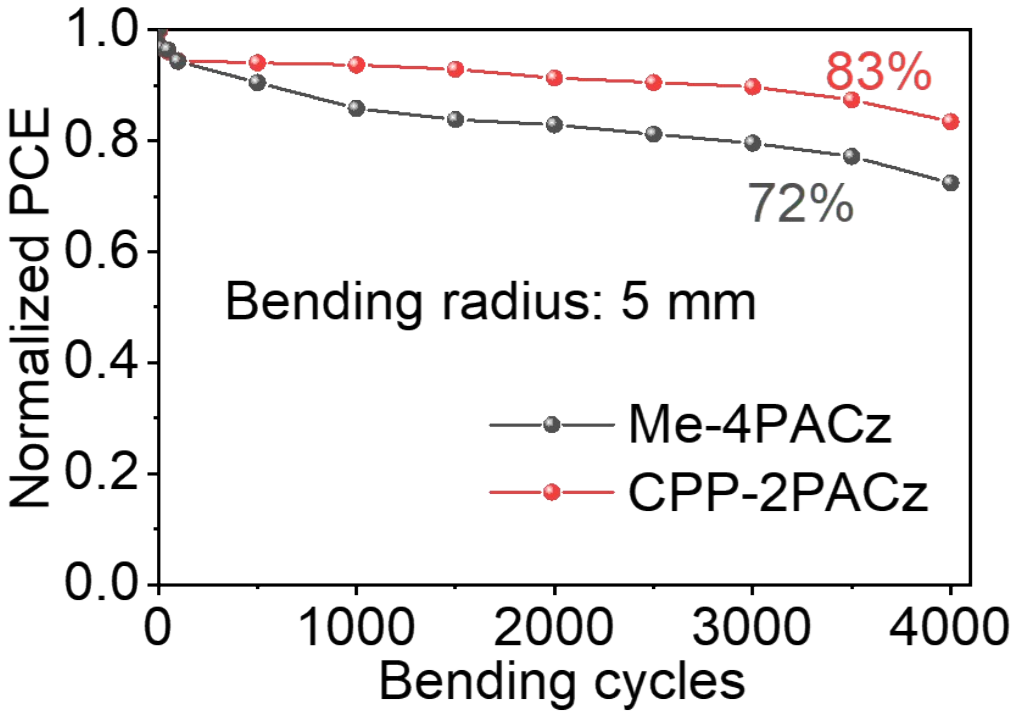

Figure S17. The normalized PCE of F-PSCs as a function of bending cycles. The device structure is PEN|ITO|NiO_x|SAMs|perovskite|C60|BCP|Ag.

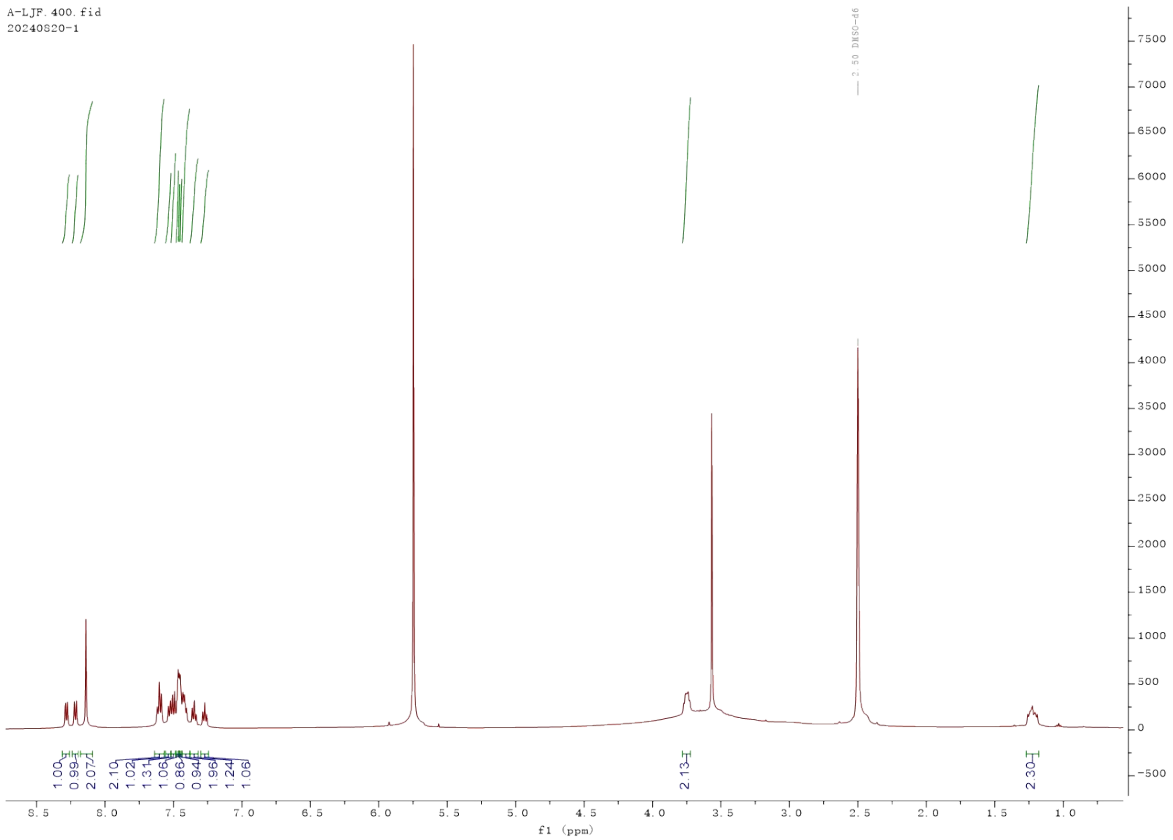

Figure S18. 1H NMR spectrum of CPP-2PACz.

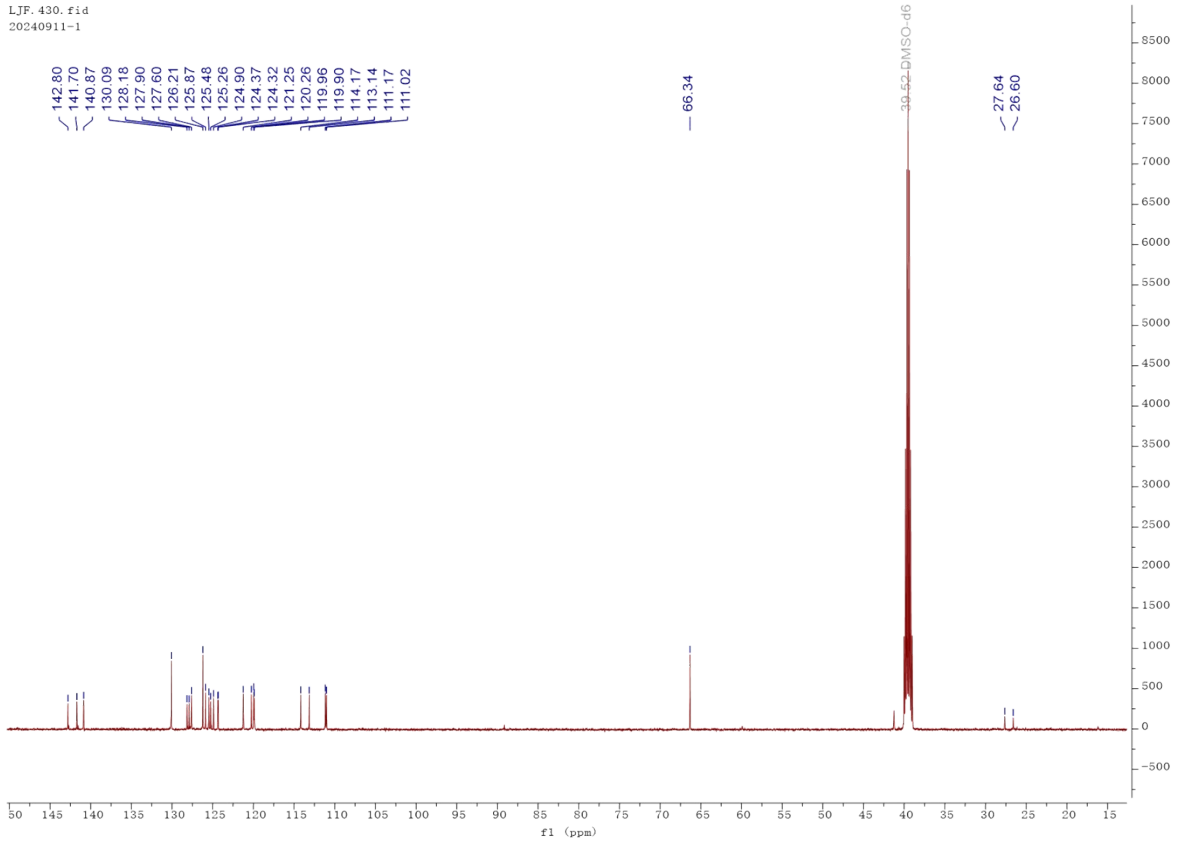

Figure S19. ^{13}C NMR spectrum of CPP-2PACz.

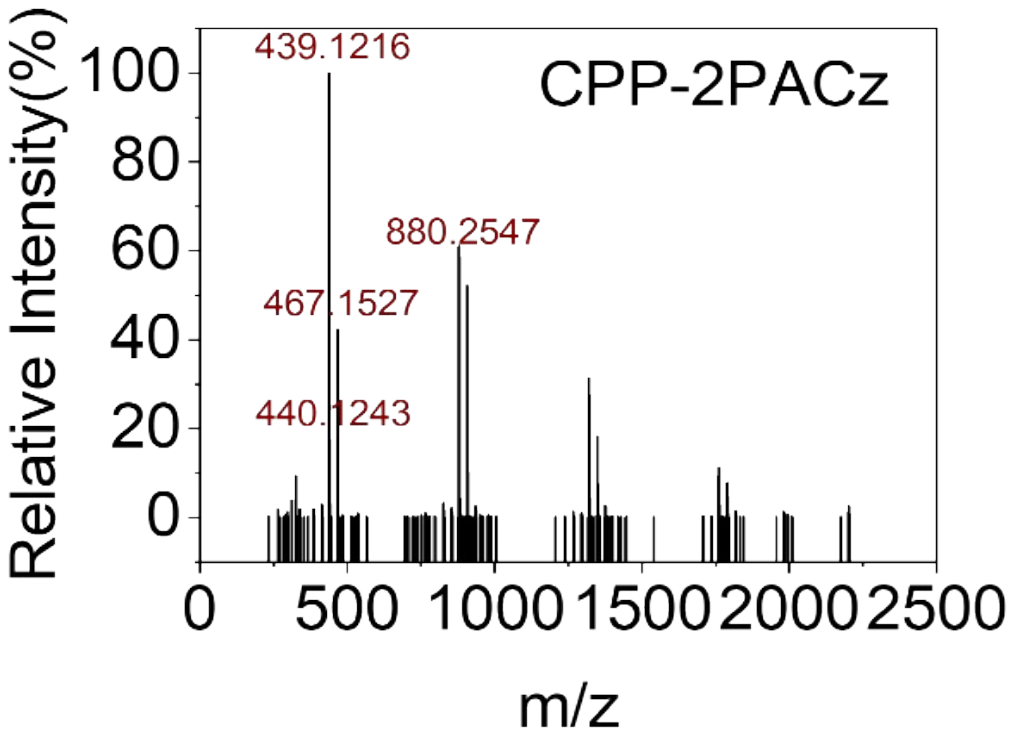

Figure S20. HRMS in negative ion mode of CPP-2PACz.

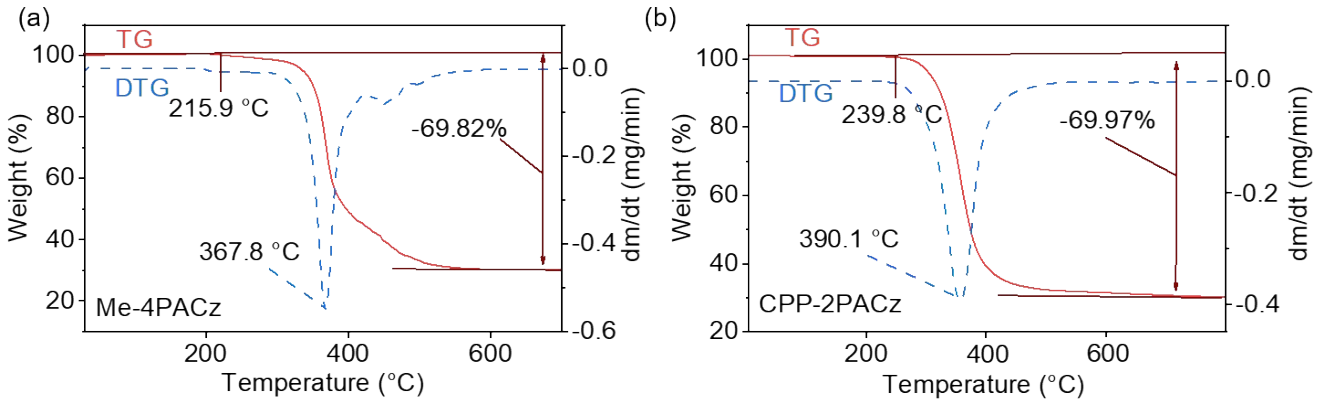

Figure S21. Thermogravimetric analysis (TGA) curve of the SAMs: (a) Me-4PACz and (b) CPP-2PACz.

Table S1. Water contact angles and $C_2H_6O_2$/CH_2I_2 contact angles of CPP-2PACz and Me-4PACz films at different annealing temperature. The sample structure is PEN|ITO|NiO_x|SAM.

Sample	liquids	80 °C	100 °C	120 °C	150 °C
CPP-2PACz	Water contact angles	87.0 ± 1.7°	83.9 ± 1.4°	82.6 ± 0.7°	83.4 ± 1.8°
	$C_2H_6O_2$ contact angles	42.5 ± 1.6°	38.4 ± 1.6°	35.2 ± 0.4°	40.7 ± 1.6°
Me-4PACz	Water contact angles	91.1 ± 3.0°	93.9 ± 1.5°	88.2 ± 0.4°	104.9 ±1.7°
	CH_2I_2 contact angles	29.0 ± 2.6°	27.9 ± 0.7°	21.9 ± 0.6°	30.3 ± 0.7°

Table S2. Parameters of the top perovskite used to fit the TPRL curves in Figure S12a, and S12c. The equation $Y=A_1\exp(-t/\tau_1) + A_2\exp(-t/\tau_2) + A_0$ and the average PL lifetime $<\tau_{avg}> = (A_1\tau 2\ 1 + A_2\tau 2\ 2)/ (A_1\tau_1 + A_2\tau_2)$. The sample structure is PEN|ITO|NiO_x|SAMs|perovskite.

Sample	Annealing temperature	τ_1(ns)	A_1(%)	τ_2(ns)	A_2(%)	τ_{avg}(ns)
Me-4PACz	80 °C	49.9	43.3	256.8	56.7	230.1
	100 °C	54.8	39.2	296.8	60.7	271.0
	120 °C	55.4	36.0	314.4	64.0	291.0
	150 °C	37.0	49.5	196.0	50.4	171.1
CPP-2PACz	80 °C	90.9	61.3	271.1	38.7	208.5
	100 °C	110.3	36.3	319.8	63.7	285.4
	120 °C	123.1	31.9	355.4	68.1	323.0
	150 °C	106.2	51.9	273.5	48.1	224.1

Table S3. Parameters of bottom perovskite used to fit the TPRL curves in Figure S12b, and S12d. The equation $Y=A_1\exp(-t/\tau_1) + A_2\exp(-t/\tau_2) + A_0$ and the average PL lifetime $<\tau_{avg}> = (A_1\tau 2\ 1 + A_2\tau 2\ 2)/ (A_1\tau_1 + A_2\tau_2)$.

Sample	Annealing temperature	τ_1(ns)	A_1(%)	τ_2(ns)	A_2(%)	τ_{avg}(ns)
Me-4PACz	80 °C	6.1	11.1	276.9	88.9	276.2
	100 °C	12.0	13.2	290.7	86.7	288.9
	120 °C	16.4	12.3	310.2	87.6	308.0
	150 °C	14.2	13.9	286.6	86.0	284.4
CPP-2PACz	80 °C	13.1	14.2	275.6	85.8	273.6
	100 °C	20.0	13.4	293.1	86.6	290.2
	120 °C	21.9	16.3	320.6	83.7	316.7
	150 °C	17.4	14.7	286.1	85.2	283.4

References:

1. G. E. Eperon, S. D. Stranks, C. Menelaou, M. B. Johnston, L. M. Herz and H. J. Snaith, *Energy Environ. Sci.,* 2014, **7**, 982–988. http://doi.org/10.1039/C3EE43822H.
2. J. Lu, L. Jiang, W. Li, F. Li, N. K. Pai, A. D. Scully, C. M. Tsai, U. Bach, A. N. Simonov, Y. B. Cheng and L. Spiccia, *Adv. Energy Mater.*, 2017, **7**. http://doi.org/10.1002/aenm.201700444.
3. J. Restolho, J. L. Mata and B. Saramago, *J. Colloid Interface Sci.*, 2009, **340**, 82–86. https://doi.org/10.1016/j.jcis.2009.08.013.
4. G. Whyman, E. Bormashenko and T. Stein, *Chem. Phys. Lett.*, 2008, **450**, 355–359. https://doi.org/10.1016/j.cplett.2007.11.033.
5. G. Bonfante, S. Chevalliot, B. Toury, B. Berge and M. Maillard, *Phys. Chem. Chem. Phys.*, 2017, **19**, 3214–3218. http://doi.org/10.1039/C6CP07392A.
6. Y. Wang, Y. Zhang, N. Teng, X. Hou, B. Duan, T. Lv, M. Hu, W. Yin, J. Lu, Solar RRL, submitted.